

Haruhiro Shiraishi¹, Yuichiro Usuda²

Real-Time Building-Damage-Extraction Technology from Ground-Based Video Footage Using Normalized Difference Red/Green Redness Index


Abstract: When an earthquake occurs, promptly identifying the presence or absence of damage is crucial. This study developed a real-time building-damage-extraction technique using ground-based imagery and evaluated its effectiveness. The technique applies the redness index (RI) (which was previously used in remote-sensing corrections for vegetation in arid regions) to identify “building damage” in those cases where buildings are partially or completely destroyed by earthquakes or tsunamis.


To capture near-field and distant perspectives in the images, each image was divided into four quadrants (upper-left, upper-right, lower-left, and lower-right). The lower-left and lower-right quadrants were analyzed to assess the conditions on either side of a road in the near field using image recognition. Since the images contain latitudinal and longitudinal information, mapping the damage along the road can be automated by recording the route. Finally, a comparative analysis with other indices was conducted in order to evaluate RI’s superiority in damage mapping. The EMS-98 damage scale was used for damage assessment, classifying D5 ($RI \geq 0.08$) as “building-collapse damage” and D0–D4 as “no building-collapse damage.” The average damage values for D5-classified buildings were significantly higher than others, thus demonstrating that RI provides practical and reliable results. Additionally, the study discussed comparisons with other indices and real-time evaluation methods. The authors sincerely hope this research contributes to life-saving efforts and deliveries of relief supplies in the aftermaths of earthquakes, ultimately saving many lives.

Keywords: earthquake, house damage, remote sensing

Received: October 9, 2024; accepted: January 15, 2025

2025 Author(s). This is an open-access publication, which can be used, distributed, and reproduced in any medium according to the Creative Commons CC-BY 4.0 License

¹ University of Tsukuba, Graduate School of Science and Technology Degree Programs in Systems and Information Engineering, Tsukuba, Japan, email: ryoma.haruhiko@gmail.com (corresponding author),  <https://orcid.org/0000-0002-2585-9335>

² University of Tsukuba, Graduate School of Science and Technology Degree Programs in Systems and Information Engineering, Tsukuba, Japan, email: usuyu@bosai.go.jp,  <https://orcid.org/0000-0002-8660-7270>

1. Introduction

1.1. Application of Remote-Sensing Indices for Extracting Building Damage and Current Challenges

Remote-sensing technologies such as satellite imagery and UAVs (unmanned aerial vehicles) are widely used to assess damage conditions following earthquakes and tsunamis; however, these methods often face challenges in accurately evaluating situations due to constraints like weather conditions, image resolutions, and coverage areas. Furthermore, generating 3D images or conducting anomaly detection requires advanced software, which can be inefficient in terms of time and cost at disaster sites [1–5].

One potential solution to these challenges is a method of capturing video footage while moving through disaster-affected areas using vehicles to rapidly identify damaged areas [6]. This approach emphasizes the importance of obtaining high-resolution and accurate images in short amounts of time using dashcams, digital cameras, or smartphones and efficiently sharing this information.

During the 2024 Noto Peninsula earthquake, for instance, the National Research Institute for Earth Science and Disaster Resilience (NIED) published images of the disaster-affected areas that were captured with a 360-degree camera that was mounted on a vehicle [7]. Moreover, advancements in platforms like Google and social media (e.g., X) have contributed to the big-data phenomenon in disaster-related imagery and videos. Consequently, it is a societal demand to eliminate irrelevant information and share accurate data swiftly [8–11].

Additionally, human vision perceives colors based on the reflectance characteristics of red, blue, and green wavelengths, and remote-sensing indices in the visible light spectrum have been studied using these properties. For example, the Visible Atmospherically Resistant Index (VARI), a vegetation index that leverages the characteristic that green reflectance is high while red reflectance is low [12]. Similarly, the Visible Water Resistant Index (VWRI), a vegetation index for representing chlorophyll concentrations in water has been developed [13, 14].

Among these, RI, which is used for correcting vegetation indices such as NDVI [15–17], has drawn attention as a method for adjusting vegetation assessments in arid regions. This study explores whether RI can be applied as a suitable index for assessing earthquake-damage conditions.

However, several challenges arise when applying RI directly to images that are obtained from disaster sites. The first issue is the inability to accurately capture positional information due to the lack of depth perception in the images. The second issue is that RI is highly responsive to artificial red objects (such as red roofs or paint in affected areas). The third issue lies in the difficulty of establishing appropriate evaluation criteria. This study addresses these challenges in an effort to develop a viable solution.

Details regarding the characteristics of spectral reflectance are shown in Figure 1.

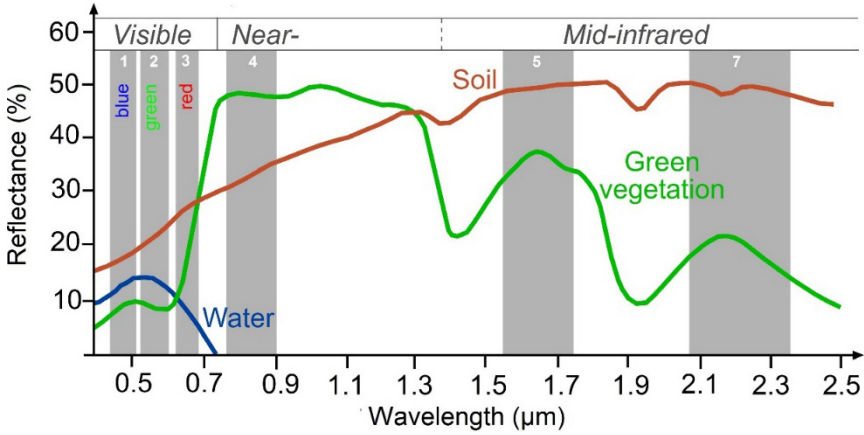


Fig. 1. Wavelength rates by physical properties (water, vegetation, soil)

Source: [18]

Vegetation equation has the following form:

$$VARI = \frac{G - R}{G + R - B} \tag{1}$$

Formula for calculating chlorophyll-a concentration in water is as follows:

$$VWRI = \frac{G - R - B}{G + R + B} \tag{2}$$

RI is expressed by the formula:

$$RI = \frac{R - G}{R + G} \tag{3}$$

1.2. Differences from Previous Studies

To date, research that has utilized satellite and aerial imagery has been conducted in efforts to automate the detections of changes before and after disasters. For instance, Tomowski et al. applied a method that was based on principal-component analysis and histogram optimization in order to visualize any changes in the images of the Haitian earthquake region before and after the disaster in 2024 [19]. Similarly, Yamazaki et al. identified regions that were affected by the Indian Ocean tsunami by comparing pre- and post-disaster images [20]. Furthermore, Ma et al. developed a series of novel methods, including the optimizable variational model (OptVM) and the scale-invariant feature transform constrained optical flow method (SIFT-OFM), to create products such as cloud-free base maps and disaster-area-change-detection maps [21].

A common feature of these studies is their reliance on comparing two images that have been captured before and after a disaster to detect any changes. In these methods, areas of missing data are influenced by a combination of spatial conditions (e.g., weather or aerial coverage) and temporal conditions (e.g., the timing of an image capture) [22, 23].

In contrast, the study that is proposed in this paper demonstrates that it is possible to estimate the extent of damage through image recognition – even when only post-disaster images are available. By using RGB data and avoiding neural networks [24] or machine learning, the resulting computational loads are significantly reduced. Additionally, this system is compatible with dashcam images, thus allowing damage-estimation results to be obtained promptly with field-survey images alone. This capability to detect affected areas in real time sets it apart from traditional approaches.

2. Methods

2.1. Flow

The overall flow is shown in Figure 2. Briefly summarized, this paper follows the following three steps.

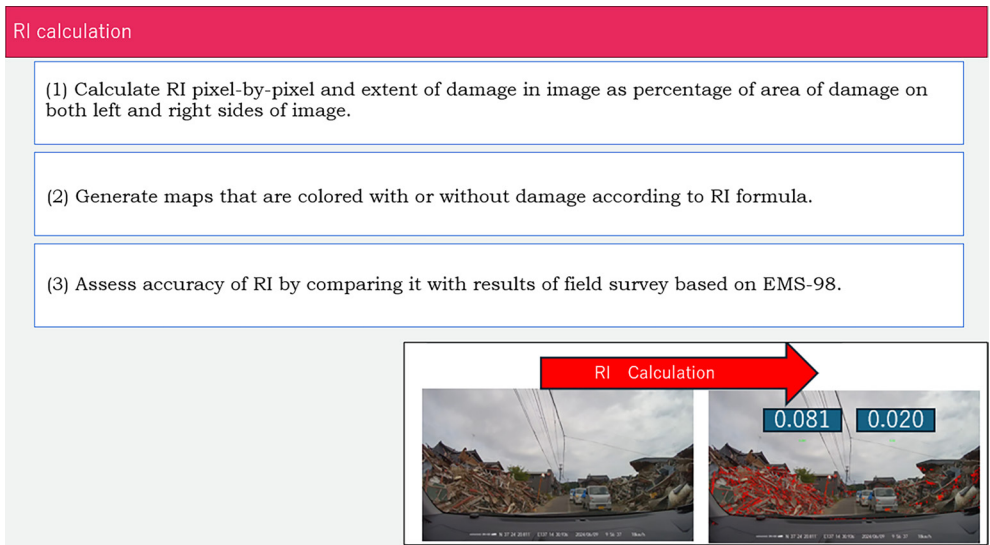


Fig. 2. Overall flow

2.2. Application of Redness Index (RI)

The redness index is calculated based on the differences in the reflectance intensity. Since soil and wood exhibit higher red reflectance and lower green reflectance, this study utilized RI as an indicator for evaluating building collapses. Assuming

that RI (which was originally developed as a vegetation-correction index for arid regions) can detect the outflow of wood and soil that is caused by building collapses or other disasters based on their spectral reflectance characteristics, this study evaluates its accuracy and utility.

RI values are obtained across the image. The mean and standard deviations of the RI values are then calculated for all of the pixels, and these values are used to classify each area as “damaged” or “not damaged.” To validate the calibration process, this study employed two methods for determining whether an area is “damaged” or “not damaged”:

- 1) calculation based on mean values,
- 2) calculation based on proportion of pixels that meet specific RI conditions.

Calculation Based on Mean Values

The average RI value for each image is calculated; if this average exceeds a specified threshold, the area is classified as “damaged.” This method aligns with the existing RI-calculation techniques.

Calculation Based on Proportion of Pixels That Meet Specific RI Conditions

To account for local sunlight and weather conditions, RI was calibrated to match the local characteristics of wood and soil. The calibrated values are referred to as RI_{cal}, and the pixels in the target image are classified as “damaged pixels” if their RI values fall within a range that is defined by the mean (μ) and standard (σ) deviations of RI_{cal}, as shown in Equations (4):

$$\mu - \alpha\sigma \leq \text{RI} \leq \mu + \alpha\sigma \quad (4)$$

An example of the image that was used for calibration is shown in Figure 3; this was selected at the discretion of the researchers.



Fig. 3. Example of debris used for calibration

2.3. Image-Segmentation Method for RI Calculation

As shown in Figure 4 (in images that were captured from a road), it is intuitively understood that the upper half of the image (namely, Regions [1] and [2]) depicts distant areas or the sky; therefore, it is reasonable to exclude the upper half of an image when analyzing nearby surroundings. The image is then divided into the lower-left and lower-right halves (referred to as Regions [3] and [4]). If RI effect is significant on either side, the image is classified as a “damaged image.” This approach ensures accurate classifications – even in those cases where only one side of a road shows collapsed buildings. This segmentation method was applied to both the mean-based calculation method and the area-based method.

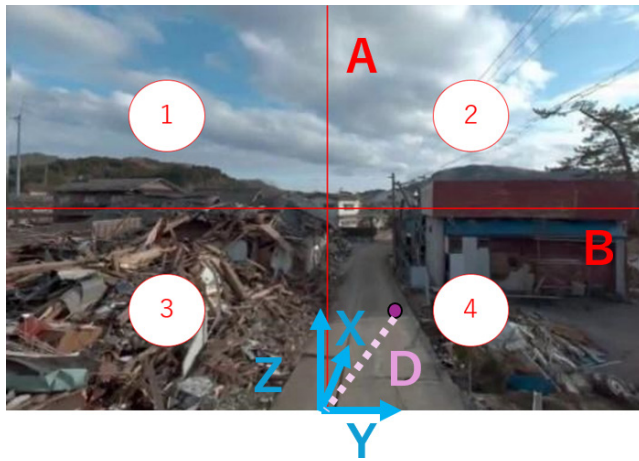


Fig. 4. Image of affected area divided into top, bottom, left, and right portions

The theoretical background for dividing the image into upper and lower as well as left and right is based on the formula for straight-line distance in three-dimensional space ($D = \sqrt{x^2 + y^2 + z^2}$). As is shown in Figure 4, Dividing Line A for the upper and lower regions corresponds approximately to the horizon. It can be visually understood that the closer an area is to the intersection of Centerline A (horizontal) and Centerline B (vertical), the further away the scene that is depicted in the image.

If the shooting position is considered to be the origin, the straight-line distance in the image can be calculated. The depth dimension of the image is evenly divided by the actual length in the depth direction (x). It becomes apparent that the length in the depth direction decreases as it approaches the intersection of A and B (which represents distant scenes). Similarly, the lengths in the horizontal (y) and vertical (z) directions also decrease as they approach the intersection of Centerlines A and B.

Using these image characteristics, it is evident that the further away an area is from the intersection of Centerlines A and B, the smaller the straight-line distance values become; this indicates the proximity to the shooting location.

The purpose of using RI is to detect and map collapsed buildings; therefore, any collapsed buildings near a shooting location would have smaller values in the vertical direction (z) as well as smaller values in the depth (x) and horizontal (y) directions. This minimizes any errors in the latitude and longitude calculations.

For images that have been captured by a dashcam, the road typically corresponds to the area near the intersection of Centerlines A and B (distant regions); these are excluded from the analysis. Hence, dividing the lower half of the image into left and right sides and evaluating each side of the road without complex calculations is deemed to be a more efficient method for obtaining results while minimizing computational load.

2.4. Comparison between Field-Survey Results and Calibrated RI

During the 2024 Noto Peninsula earthquake, more than 100,000 buildings were damaged [25]. Based on field survey results by Naito et al. [26], the proportion of the RI areas was compared with the five damage levels that are defined by EMS-98 [27] to determine whether D5 could be appropriately evaluated as “building-collapse damage.”

3. Results

The authors attempted to estimate the scale of damage using two methods based on the RI. The first method involves calculating the average RI value for each image and classifying it as “damaged” if the average value exceeds a specified threshold; this approach is considered to yield results that are generally consistent with traditional RI calculation methods. The second method classifies an image as “damaged” if the proportion of the RI values that meet damage conditions exceeds a certain area ratio.

The results revealed three key differences between the classification method based on the proportion of the calibrated RI areas and the method that was based on the average RI values. These differences demonstrated that calibration outperformed the traditional approach in all aspects; the details of this assertion are outlined in Sections 3.1 through 3.3.

3.1. Standardization of Damage Scale Based on Imaging Conditions

The damage-scale-evaluation method that uses the average RI value for each pixel is limited by imaging conditions such as light intensity, weather, and regional characteristics. To address this issue, this study employed RI calibration; specifically, this calibration used images of eroded soil and wood that were specific to the local terrain and weather conditions, enabling the standardization of the damage scale under these conditions.

Following the calibration, those pixels with RI values that were close to the reference image were classified as “damaged pixels” (*A*), while those that were far from the reference were classified as “non-damaged pixels” (*B*). The proportion of “damaged pixels” relative to the total number of pixels ($V = A/[A + B]$) was then calculated to quantitatively evaluate the damage scale. This approach allowed for highly accurate calculations and a quantitative representation of the damage scale.

For example, the pre-calibration image failed to accurately calculate the partial damage to the building on the right side (as is shown in Figure 5). In the post-calibration image, however, the proportion of the “damaged pixels” in the lower-left region was calculated to be 0.001 (0.1%), while the lower-right region showed a proportion (*V*) of 0.087 (8.7%). These results clarified the quantitative criteria for damage classification and demonstrated the improved accuracy in identifying “damaged pixels.”

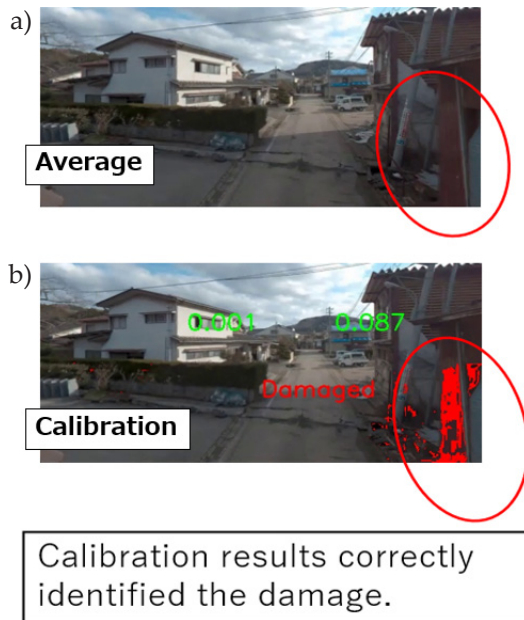


Fig. 5. Value calculated by average of RI (red area should indicate heavily damaged area, but it is, in fact, not shown correctly) (a); value calculated after calibration of RI (b)

3.2. Automation of Thresholds

When setting thresholds by using the average RI value, a manual determination of the threshold is required; this manual process can lead to significant time consumptions for damage-scale calculations. When using the proportion of the RI areas (*V*) after calibration, however, the process can be automated by employing the mean (μ) and standard deviation (σ) of the pixel values.

Specifically, the proportion of the RI areas (V) is defined within a range that is determined by α times the standard deviation (σ) from the mean (μ) of the pixel values in the calibration image. This approach enables one to determine that the closer the RI value is to the calibration image, the greater the damage scale, and the further away it is, the smaller the damage scale. Here, coefficient α is a value that is chosen arbitrarily by the experimenter. The proportion of the RI areas (V) is determined based on the standard normal distribution table for a given α . For instance, when α is set to 1, the proportion of the RI areas (V) is set at 0.68 (based on the standard normal distribution table).

According to the authors' experimental results, setting α to 0.1 and the proportion of the RI areas (V) to 0.08 enables an accurate approximation of α to the true threshold.

3.3. Accuracy in Identifying Damage Conditions

Calculations using the average RI value have often resulted in the misidentifications of damage conditions. For instance, the red car in the lower-left corner was incorrectly classified as "damaged" based on the average RI value (as shown in Figure 6). In contrast, when the calibrated index was used to calculate the proportion (V) of the total area, the system correctly identified the car as "no damage."

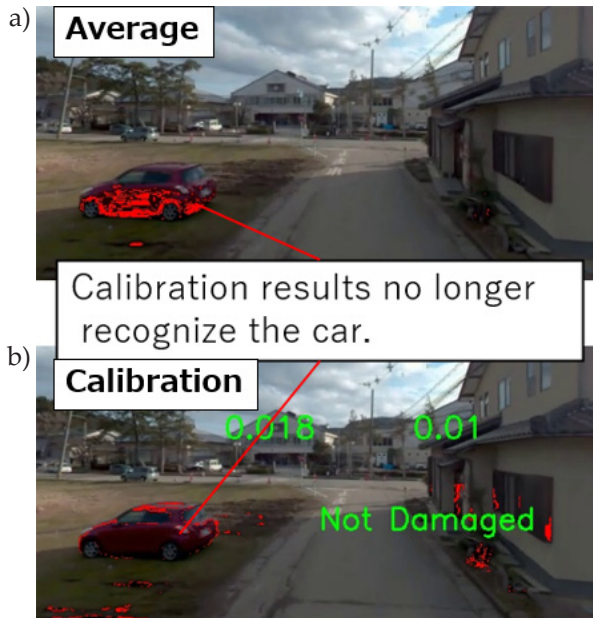


Fig. 6. Example of misidentification as "damaged" by average RI value (a); example of correctly identifying "no damage" to car using proportion of RI area after calibration (b)

3.4. Comparison of Automatically Generated “Damaged” Maps and Field-Survey Results

Using geotagged images, an automatically generated map was created in order to identify “damaged” areas based on the standard normal distribution table (where values of 0.08 [0.1 σ] or higher were classified as “damaged”). As a result, D5- and D5+ were accurately identified as “damaged” (as shown in Figure 7).

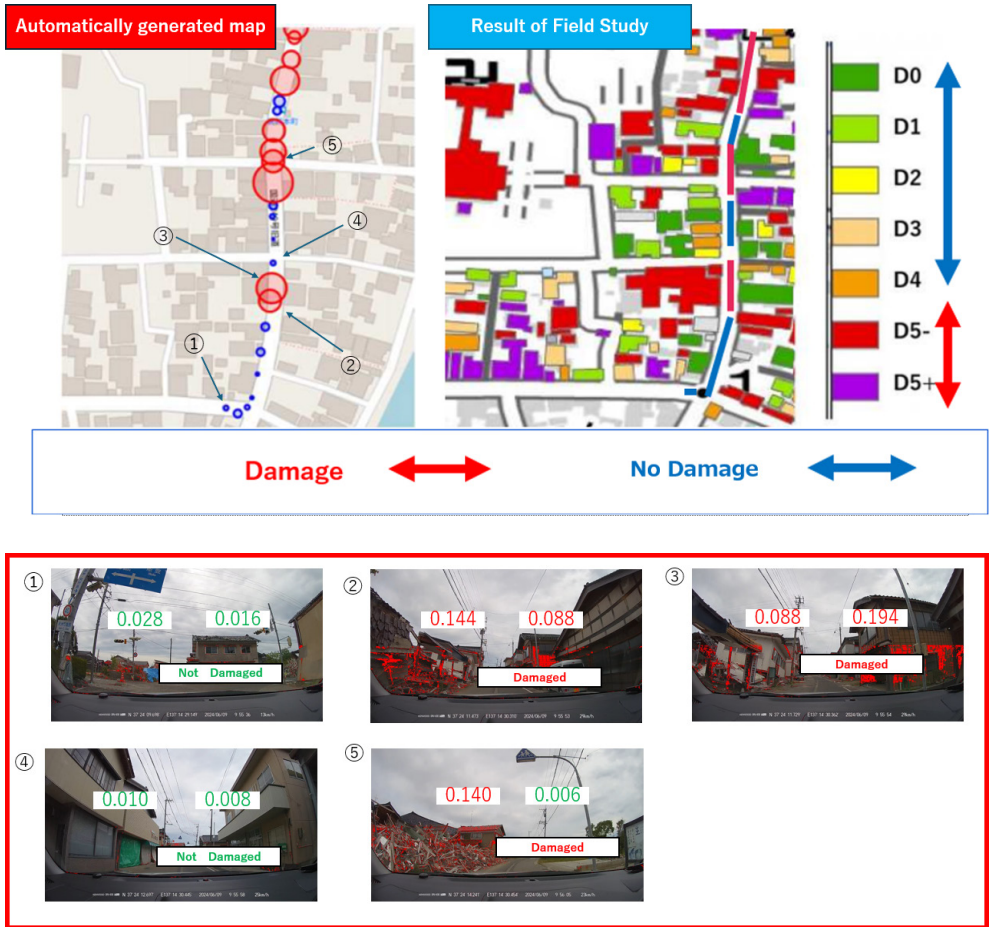


Fig. 7. Comparison of automatically generated “damaged” map (left) and field-survey results (right)

Furthermore, the lower half of the image was obscured by the vehicle’s front end, and a correction factor of 2.0 was applied to calculate the proportion of “damaged pixels” that were used in the results (as illustrated in Figure 8).



Fig. 8. Image with lower area obscured by front end of vehicle

3.5. Results of RI Calculation

Those pixels that met the calibration conditions were marked in red. An area was classified as “damaged” if one side of the image contained more than 0.08 of the total proportion. This criterion corresponded to D4–D5 on the EMS-98 scale and was considered to be suitable for the early detection of and rapid response to residential damage.

The following explain the results of the five images that are shown in Figure 7:

- **Image ①.** The proportions of the building damage on both the left and right edges were 0.028 and 0.016, respectively, thus resulting in a prediction of “no damage” for both sides. The field survey confirmed that this prediction was correct, with no damage (D0) being reported. Even though minor damage appeared in the distant area, the estimation method effectively excluded distant areas, accurately focusing on nearby damage.
- **Image ②.** The proportions of the building damage on the left and right sides were 0.144 and 0.088, respectively, thus predicting “damaged” for both sides. The field-survey results confirmed that the left building was D5– while the right building was D0. The right building was mistakenly classified as “damaged” due to its slightly reddish-brown color, which caused a false positive.
- **Image ③.** Similar to Image ②, the right building (with its reddish-brown color) was misclassified as “damaged.” Addressing areas with prominent red tones has been identified as a challenge for future research.
- **Image ④.** Both sides were predicted as “no damage,” which was consistent with the field survey that confirmed no damage in the area.
- **Image ⑤.** The left side was predicted as “damaged,” and the right side was predicted as “no damage.” The field survey confirmed that only the left side was damaged, thus demonstrating the accuracy of the damage detection.

For actual damage scales, the average proportion of “damaged pixels” gradually increased across the D0 to D4 categories. In contrast, the proportions increased significantly for D5– and D5+, reaching very high values of 0.138 and 0.136, respectively. Since D5– and D5+ are collectively referred to as D5 in the EMS-98 standard, the statistics were also calculated as D5. These results showed that the proportion of “damaged pixels” increased significantly when buildings collapsed; this indicated that this index is highly effective for measuring severe damage.

Even in the lower-damage categories, a gradual upward trend could be observed; this suggested that the index had sufficient accuracy for the early identification of significant damage. Among the 15 buildings that were classified as D5 (collapsed), 14 were correctly identified as “damaged.” Additionally, 14 non-collapsed buildings were accurately classified as “no damage” among the 16 buildings (D0–D4) (Table 1).

Table 1. Mean and standard deviation of RI compared to damage in Suzu City, Ishikawa Prefecture, during Noto Peninsula earthquake

Damage situation	Average of area percentage of RI	Standard deviation of RI
D0	0.016	0.014
D1	0.044	0.032
D2	0.032	0.000
D3	0.060	0.010
D4	0.074	0.064
D5	0.138	0.052
D5–	0.136	0.056
D5+	0.134	0.030

4. Discussion

4.1. Calculation of 0.1σ and 8% Value

From the calibrated images, those values that exceeded 0.1σ (standard deviation) and represented 8% of the total area were calculated using the combined theoretical values from both sides of the normalized standard deviation table. The standard deviation (σ) reflected the deviation, and those areas that satisfied the calibration conditions for local sunlight and weather were considered “damaged.”

4.2. Calibration Images

When images that were unrelated to the affected areas were used for calibration, a significant drop in the accuracy could be observed (as shown in Figure 9). This highlighted the importance of conducting one’s calibrations based on regional standards.



Fig. 9. Example of accuracy degradation when using unrelated images for calibration

4.3. Acceleration of Damage Assessment Using Geotagged Images and Mapping

Using the burst mode of a smartphone camera allows for multiple still images to be saved with GPS information. By comparing the damage-detection results in images with GPS data, precise location information for D5 damage on the EMS-98 scale can be provided. Additionally, larger RI area ratios indicate potentially greater damage, thus suggesting the feasibility of generating quantitative maps. Rapid damage assessment facilitates the sharing of information on affected locations and provides guidance for safe actions. In initial responses, the ability to reduce the extents of human and property losses (and quickly communicate this information) is critical. By quantitatively calculating damage levels, it becomes possible to rapidly communicate and accurately identify “when” something happened, “where” it happened, and “what” exactly happened.

4.4. Application Studies of RI Index

Chen et al. revealed that, in the context of cotton verticillium wilt (one of the most widespread cotton diseases in China and worldwide), the RI value showed the highest positive correlation ($R^2 = 0.524$) with the disease severity and spectral indices among conventional survey methods [28]. Additionally, RI has been shown to be practical and highly accurate for monitoring, thus demonstrating its high applicability in the agricultural sector.

On the other hand, there are no confirmed studies that have applied RI in the field of disaster management as far as the authors have investigated; this suggests that this is an area with significant potential for future research advancements.

5. Conclusion

This study focused on developing a method for swiftly extracting “damage” information from disaster-site imagery. The results demonstrated that RI could effectively assess the scales of building collapses that are caused by earthquakes. The novelty of this study lies in developing an image-recognition technique that minimizes computational loads by using only RGB values without relying on machine-learning or neural networks.

A comparison with field surveys confirmed the fact that this index could quantitatively evaluate disaster scales through the calibrations of disaster-site images. The maps that were generated using this index were sufficiently accurate for detecting damaged buildings: 14 of 15 buildings that were classified as D5 (collapsed) were correctly identified as “damaged,” and 14 of 16 non-collapsed buildings (D0–D4) were accurately classified as “not damaged.”

According to EMS-98, D5 (corresponding to $RI \geq 0.08$) is classified as “building-collapse damage,” while D0–D4 are classified as “no building collapse.” The average RI value for the D5-damaged buildings in our study was 0.136, which was significantly higher than other categories; this confirmed that the damage was correctly recognized.

This analytical approach is highly effective for initial responses that require rapid action. Ultimately, the authors aimed to apply this index in participatory GIS and public or mutual-aid systems. It is hoped that the use of this index will enable a quicker understanding of the safety and damage conditions that typically follow disasters.

Funding

This work was supported by JST SPRING, Japan Grant Number JPMJSP2124.

CRedit Author Contributions

H. S.: conceptualization, methodology, software, validation, formal analysis, investigation, resources, data curation, writing – original draft preparation, writing – review and editing, visualization, funding acquisition.

Y. U.: conceptualization, validation, supervision, project administration.

All of the authors have read and agreed to the published version of the manuscript.

Declaration of Competing Interests

The authors declare that they have no known competing financial interests or personal relationships that could have appeared to influence the work reported in this paper.

Data Availability

Not applicable.

Use of Generative AI and AI-Assisted Technologies

No generative AI or AI-assisted technologies were employed in the preparation of this manuscript.

Acknowledgements

This work was supported by JST SPRING, Japan Grant Number JPMJSP2124. Dr. Yoshinobu Mizui (REIC) provided advice on estimating disaster situation from photographs and gave us the photo data on this research. We also thank Iwane Laboratories, LTD, for their advice on the analytical methods. We would like to express our gratitude to Dr. Shohei Naito for his given field-survey results.

References

- [1] Hiroo K.: *Mechanism of tsunami earthquakes*. Physics of the Earth and Planetary Interiors, vol. 6(5), 1972, pp. 346–359. [https://doi.org/10.1016/0031-9201\(72\)90058-1](https://doi.org/10.1016/0031-9201(72)90058-1).
- [2] Okamoto T., Takenaka H., Nakamura T., Hara T.: *FDM simulation of earthquakes off western Kyushu, Japan, using a land-ocean unified 3D structure model*. Earth, Planets and Space, vol. 69, 2017, 88. <https://doi.org/10.1186/s40623-017-0672-9>.
- [3] Chen J., Liu H., Zheng J., Lv M., Yan B., Hu X., Gao Y.: *Damage degree evaluation of earthquake area using UAV aerial image*. International Journal of Aerospace Engineering, vol. 2016(1), 2016, 2052603. <https://doi.org/10.1155/2016/2052603>.
- [4] Voigt S., Kemper T., Riedlinger T., Kiefl R., Scholte K., Mehl H.: *Satellite image analysis for disaster and crisis-management support*. IEEE Transactions on Geoscience and Remote Sensing, vol. 45(6), 2007, pp. 1520–1528. <https://doi.org/10.1109/TGRS.2007.895830>.
- [5] Chandola V., Banerjee A., Kumar V.: *Anomaly detection: A survey*. ACM Computing Surveys (CSUR), vol. 41(3), 2009, 15. <https://doi.org/10.1145/1541880.1541882>.
- [6] Mizui Y., Fujiwara H.: *Estimate the amount of disaster waste disposal work using in-vehicle camera images – a case study in Hitoyoshi City, Kumamoto Prefecture*. Journal of Disaster Research, vol. 16(7), 2021, pp. 1061–1073. <https://doi.org/10.20965/jdr.2021.p1061>.
- [7] 2024 Noto earthquake bosaiXview. <https://xview.bosai.go.jp/view/index.html?appid=41a77b3dcf3846029206b86107877780> [access: 16.01.2025].
- [8] Li X., Cheng X., Chen W., Chen G., Liu S.: *Identification of forested landslides using LiDar data, object-based image analysis, and machine learning algorithms*. Remote Sensing, vol. 7(8), 2015, pp. 9705–9726. <https://doi.org/10.3390/rs70809705>.
- [9] Anwar S.M., Majid M., Qayyum A., Awais M., Alnowami M., Khan M.K.: *Medical image analysis using convolutional neural networks: a review*. Journal of Medical Systems, vol. 42, 2018, 226. <https://doi.org/10.1007/s10916-018-1088-1>.

- [10] Koskosidis Y.A., Powell W.B., Solomon M.M.: *An optimization-based heuristic for vehicle routing and scheduling with soft time window constraints*. Transportation Science, vol. 26(2), 1992, pp. 69–85. <https://doi.org/10.1287/trsc.26.2.69>.
- [11] Taniguchi E., Yamada T., Kakimoto Y.: *Probabilistic vehicle routing and scheduling with variable travel times*. IFAC Proceedings, vol. 33(9), 2000, pp. 33–38. [https://doi.org/10.1016/S1474-6670\(17\)38119-3](https://doi.org/10.1016/S1474-6670(17)38119-3).
- [12] Gitelson A.A., Stark R., Grits U., Rundquist D., Kaufman Y., Derry D.: *Vegetation and soil lines in visible spectral space: A concept and technique for remote estimation of vegetation fraction*. International Journal of Remote Sensing, vol. 23(13), pp. 2537–2562. <https://doi.org/10.1080/01431160110107806>.
- [13] Shiraishi H.: *New index for estimation of chlorophyll-a concentration in water with RGB value*. International Journal of Engineering & Technology, vol. 18(6), 2018, pp. 10–16.
- [14] Cobelo I., Machado K.B., David A.C.M., Carvalho P., Ferreira M.E., Nabout J.C.: *Unmanned aerial vehicles and low-cost sensor as tools for monitoring freshwater chlorophyll-a in mesocosms with different trophic state*. International Journal of Environmental Science and Technology, vol. 20(6), 2023, pp. 5925–5936. <https://doi.org/10.1007/s13762-022-04386-3>.
- [15] Bannari A., Morin D., Bonn F., Huete A.: *A review of vegetation indices*. Remote Sensing Reviews, vol. 13(1–2), pp. 95–120. <https://doi.org/10.1080/02757259509532298>.
- [16] Escadafal R., Belghit A., Ben-Moussa A.: *Indices spectraux pour la télédétection de la dégradation des milieux naturels en Tunisie aride*, [in:] Guyot G. (éd.), *Mesures physiques et signatures en télédétection: Sixième symposium international; actes; 17–21 Janvier 1994, Val d’Isère, France: Proceedings*, CNES, Centre National d’Etudes Spatiales, Paris 1994, pp. 253–259.
- [17] Escadafal R., Huete A.: *Étude des propriétés spectrales des sols arides appliquée à l’amélioration des indices de végétation obtenus par télédétection [Improvement in remote sensing of low vegetation cover in arid regions by correcting vegetation indices for soil “noise”]*. Comptes Rendus de l’Académie des Sciences. Serie 2, vol. 312(11), 1991, pp. 1385–1391.
- [18] SEOS: *Classification Algorithms and Methods*. <https://seos-project.eu/classification/classification-c01-p05.html> [access: 16.01.2025].
- [19] Tomowski D., Ehlers M., Klonus S.: *Colour and texture based change detection for urban disaster analysis*, [in:] *2011 Joint Urban Remote Sensing Event, Munich, Germany, 2011*, IEEE, Piscataway 2011, pp. 329–332. <https://doi.org/10.1109/JURSE.2011.5764786>.
- [20] Yamazaki F., Matsuoka M.: *Remote sensing technologies in post-disaster damage assessment*. Journal of Earthquake and Tsunami, vol. 1(3), 2007, pp. 193–210. <https://doi.org/10.1142/S1793431107000122>.
- [21] Ma Y., Chen F., Liu J., He Y., Duan J., Li X.: *An automatic procedure for early disaster change mapping based on optical remote sensing*. Remote Sensing, vol. 8(4), 2016, 272. <https://doi.org/10.3390/rs8040272>.

- [22] Ren Y., Liu Y.: *Geological disaster detection from remote sensing image based on experts' knowledge and image features*, [in:] 2016 IEEE International Geoscience and Remote Sensing Symposium (IGARSS), Beijing, China, 2016, IEEE, Piscataway 2016, pp. 677–680. <https://doi.org/10.1109/IGARSS.2016.7729170>.
- [23] Ye S., Nourzad S.H.H., Pradhan A., Bartoli I., Kontsos A.: *Automated detection of damaged areas after hurricane sandy using aerial color images*, [in:] Issa R.R., Flood I. (eds.), *Computing in Civil and Building Engineering: Proceedings of the 2014 International Conference on Computing in Civil and Building Engineering: June 23–25, 2014, Orlando, Florida*, American Society of Civil Engineers, Reston 2014, pp. 1796–1803. <https://doi.org/10.1061/9780784413616.223>.
- [24] Amit S.N.K.B., Aoki Y.: *Disaster detection from aerial imagery with convolutional neural network*, [in:] 2017 International Electronics Symposium on Knowledge Creation and Intelligent Computing (IES-KCIC), Surabaya, Indonesia, 2017, IEEE, Piscataway 2017, pp. 239–245. <https://doi.org/10.1109/KCIC.2017.8228593>.
- [25] Cabinet Office Japan, Disaster Management in Japan. <https://www.bousai.go.jp> [access: 16.01.2025].
- [26] Okada S., Takai N.: *Jishin higai chōsa no tame no tatemono bunrui to higai patān* [Classifications of structural types and damage patterns of buildings for earthquake field investigation]. *Journal of Structural and Construction Engineering*, vol. 64(524), 1999, pp. 65–72. https://doi.org/10.3130/aijs.64.65_5.
- [27] Naito S., Takahashi I.: *Reiwa 6 nen noto hanto Jishin ni okeru tatemono higai no shikkai chosa oyobi koku shashin handoku tonu hikaku* [Comprehensive survey of building damage in the 2024 Noto Peninsula earthquake and comparison with aerial photograph interpretation], [in:] *Conference Proceedings of the Architectural Institute of Japan (Kanto), 2024 August*, art. no. 21121, pp. 241–242. <https://www.aij.or.jp/paper/detail.html?productId=699519>.
- [28] Chen B., Li S., Wang K., Su Y., Chen J., Jin X., Lv Y., Diao W.: *Estimating severity level of cotton disease based on spectral indices of TM image*. *Journal of Infrared and Millimeter Waves*, vol. 30(5), 2011, pp. 451–456.